Journal of Materials Research and Technology 41 (2026) 7628–7640

Contents lists available at ScienceDirect

Journal of Materials Research and Technology

journal homepage: www.elsevier.com/locate/jmrt

Molecular dynamics of NP–CNT interfaces: Interfacial interactions and structural evolution across size and temperature

Shizhen Li [a], Chenshan Gao [a], Xu Liu [b], Jieming Lin [a], Tiancheng Tian [c], Shaogang Wang [b], Huaiyu Ye [a,b,*]

[a] School of Microelectronics, Southern University of Science and Technology, Shenzhen, China
[b] Electrical Engineering, Mathematics and Computer Science, Delft University of Technology, Delft, the Netherlands
[c] The Shanghai Engineering Technology Research Centerand Advanced Manufacturing, Fudan University, of SiC Power Device, College of Intelligent Robotics, Shanghai, 200433, China

ARTICLE INFO

Handling Editor: Prof. M Meyers

Keywords:
Nanoparticle
Carbon nanotube
Interface
Wetting
Molecular dynamics

ABSTRACT

CNT–metal nanoparticle interconnects are attractive for advanced and power electronic packaging, yet the atomistic mechanisms of nanoparticle–Carbon nanotube (NP–CNT) sidewall contact remain unclear under size and temperature variations. Here, molecular dynamics simulations establish a mechanism-consistent chain linking energetics, structural evolution, CNT mechanical accommodation, stress localization, and curvature-induced anisotropy in solid-state Ag NP–CNT contact. A direct Ag NP–NP benchmark highlights the fundamental difference: NP–CNT contact shows a much weaker energetic drive and lacks diffusion-driven neck growth. Therefore, interfacial adjustment is dominated by adsorption and coupled CNT indentation–bending–damping. Interfacial stresses concentrate near the contact boundary and penetrate into subsurface layers. Increasing temperature can reduces peak stress and broadens the stressed region. Systematic cases reveal that high temperature combined with small NP size activates late-time transient disordering followed by interface-adjacent recrystallization, producing a multi-grain, multiply twinned NP with Σ3{111}-related twins. At last the solid-state wetting analysis shows strong axial–circumferential anisotropy governed by indentation–bending coupling and cylindrical curvature. These results provide atomistic guidelines for choosing NP size, processing temperature, and CNT texture to balance adhesion, structural stability, and stress concentration.

1. Introduction

With the rapid development of advanced packaging and power electronics packaging, interconnects are increasingly required to sustain higher interconnection density, higher heat flux, and elevated junction temperatures during operation [1–3]. These harsher service conditions intensify thermomechanical fatigue in the interconnection layer, which degrades electrical and thermal performance and reduces operation life [4]. Meanwhile, the intrinsic limitations of conventional metallic interconnect materials further constrain the continuous improvement of power density and thermal management capability in modern packaging architectures [5]. Therefore, developing interconnect materials with better thermal, electrical and mechanical properties is necessary for next-generation electronic packaging.

Carbon nanotubes (CNTs) exhibit outstanding mechanical strength and excellent thermal and electrical conductivity, making them attractive candidates for enhancing packaging materials and interconnect systems [6]. In electronic packaging, CNT has been used in multiple directions, including TSV/TGV interconnects and thermal interface materials (TIMs) [7,8]. However, the effective performance is often limited by weak van der Waals coupling at inter-tube junctions; recent studies show that interface engineering can enhance interfacial heat transfer and even mitigate its temperature dependence [9,10]. Despite these promising demonstrations, the practical implementation of CNTs in packaging remains challenging, due to poor wettability on metal/-ceramic substrates, high interfacial contact resistance, and limited compatibility with conventional manufacturing flows [11–13]. These constraints motivate CNT–metal hybridization as a more process-compatible route to translate CNT advantages into engineering-relevant interconnect structures [14,15].

Accordingly, CNT–metal composites have been widely investigated to improve thermal/electrical transport and mechanical robustness in

* Corresponding author.
E-mail address: h.ye@tudelft.nl (H. Ye).

https://doi.org/10.1016/j.jmrt.2026.02.194
Received 12 January 2026; Received in revised form 16 February 2026; Accepted 23 February 2026
Available online 2 March 2026

Ag- and Cu-based joints, films, and sintered networks. For example, incorporating CNTs into nanosilver pastes has been reported to enhance joint shear strength while reducing resistivity compared with CNT-free joints [16]. and similar strategies have been extended to nanocopper sintering pastes where the performance depends strongly on CNT type, surface chemistry, and loading fraction [17]. For thermal management, functionalized CNTs combined with metal nanoparticles have also shown clear benefits in composite TIM structures [18,19]. Collectively, these experimental and materials-design advances indicate that CNTs can indeed improve interconnect performance. Despite these advances, the practical enhancement is ultimately controlled by the metal–CNT interfacial contact state and its nanoscale stress/structure evolution, which remain insufficiently understood for predictive process and interface design [11–13]. Recent studies further underscore that atomistic-level regulation of sp^2-carbon/metal interfaces can substantially affect interfacial transport and composite performance, highlighting the need for a mechanistic NP–CNT interfacial understanding under packaging-relevant conditions [20–22].

Molecular dynamics (MD) simulation provides a direct route to resolve atomic-scale interfacial processes—such as adhesion energetics, local structural rearrangement, diffusion, and stress localization—that are difficult to isolate experimentally. Prior MD studies have investigated bulk metal–CNT interfaces and related composites by analyzing interfacial energy variation, diffusion behavior, and crystal structure evolution, as well as thermal transport across engineered interfaces using non-equilibrium MD (NEMD) approaches [23,24]. Other simulations have examined CNT-induced defects and mechanical responses under strain or temperature variations, and have attempted to establish predictive relations between temperature and elastic/shear properties for specific metal–CNT systems [25,26]. While these studies mainly focus on bulk-like metal–CNT interfaces and composite behavior. These simulation systems often rely on continuous matrices or idealized interface configurations, and thus do not directly address the nanoparticle-dominated interconnect scenarios commonly encountered in electronic packaging.

In practical electronic packaging, NP systems are ubiquitous. Material properties and interfacial behavior of Ag/Cu nanoparticle-based pastes and their sintered networks can change markedly at the nanoscale. Consequently, mechanisms and trends established for bulk–CNT interfaces cannot be directly extrapolated to NP–CNT contacts. Although some NP–CNT related simulations exist, such as studies on nanoparticle insertion between CNTs to facilitate phonon transmission, nanoparticle self-assembly inside CNTs, or temperature-driven nanoparticle migration at top/bottom CNT, the majority of these scenarios do not directly capture the sidewall contact and bonding processes relevant to NP-based interconnect formation and evolution [27–29]. Moreover, a number of MD studies have investigated metal NP interactions with graphene [30–32]. However, despite both being sp^2-bonded carbon allotropes, the curvature of CNTs changes surface energetics and adsorption/wetting characteristics compared with planar graphene, potentially leading to distinct interfacial bonding and contact anisotropy [33,34]. Therefore, dedicated and systematic investigations of metal NP–CNT interfacial contact, especially under size and temperature variations, are still needed to establish an atomic-scale mechanistic basis for CNT-enabled nanoparticle interconnect design.

In this work, we focus on Ag NPs as a representative packaging-relevant system and construct an Ag NP–CNT sidewall contact model to elucidate nanoscale interfacial mechanisms. To highlight the fundamental differences between nanoparticle sintering and nanoparticle–CNT contact, a two-particle NP–NP sintering model is also employed as a reference under an identical analysis framework. We first evaluate the thermal stability of Ag NPs across sizes, and then perform a systematic comparison between NP–NP and NP–CNT contact evolution. Subsequently, the effects of temperature, NP size, contact/bonding position, and CNT defects on interfacial energetics, CNT deformation, interfacial stress distribution, and contact morphology are examined. Finally, the wetting/contact characteristics and their governing factors are discussed to provide mechanistic insights that can inform subsequent experimental design and processing-window selection for CNT–metal nanoparticle interconnects.

2. Method

2.1. Melting simulation

NPs possess high surface energy, and size effects intensify as their diameter decreases. Accordingly, the melting point becomes strongly dependent on size [35]. Different NP sizes can therefore exhibit distinct thermodynamic and kinetic behaviors that may critically influence the NP–CNT interfacial bonding mechanism. We conduct single NP melting simulations as a controlled baseline. This approach isolates the size effect, allowing us to determine the melting point at each diameter and to track how atomic order evolves with temperature. The results provide a clean reference for interpreting size-dependent behavior in subsequent NP–CNT studies.

The melting simulation includes NPs with 7 different radiuses from 2a to 8a (a is the lattice constant of silver, a = 4.09 Å). The configuration of these 7 type NPs was shown in Fig. 1 and S3. Before melting simulation, each NP first subjected energy minimization, then conducted the relaxation at 300K to ensure the NP became equilibrium. In the melting simulation, we employed the isothermal melting simulation with a temperature step of 20K from 300K to 1400K. In each temperature step, we first heat the system to the target temperature within 200ps. And keep the NP under corresponding temperature for 500ps to ensure that the system reached equilibrium. The state of NP that we chose to calculate for post process was only the last 50ps to eliminate the influence of temperature gradient.

2.2. NP-CNT interconnection simulation

In the NP-CNT interconnection simulation, wo built the double particle model refers to the conventional double metallic NP sintering model. Left side of model is NP and the other side is SWCNT. In this work the length of SWCNT was set to 152.275 Å to prevent the NP moves to the top or bottom side of CNT leading to contact position change. We adopted a (5,5) armchair SWCNT, which is metallic and highly symmetric. There are also some other CNT-related works used similar CNT [25,36]. It's very suitable for simulation. Each of them was relaxed for 500ps to make sure the single model reached equilibrium at target sintering temperature. This could eliminate the influence of temperature increasing process and temperature gradient. They were assembled with a gap of 3 Å. The NP was oriented with (100) facet facing the CNT sidewall.

2.3. Detail of simulation

The force field of the simulation system is a hybrid potential. The interaction of silver to silver was determined by Cu–Ag eam alloy potential developed by P.L. Williams, which had already been verified by many metallic NP sintering related works [37]. The total energy is defined as:

$$Ei = F_\alpha\left(\sum_{j\neq i}\rho_\beta(r_{ij})\right) + \frac{1}{2}\sum_{j\neq i}\phi_{\alpha\beta}(r_{ij}) \quad (1)$$

where F_α and $\phi_{\alpha\beta}$ are the embedding energy and potential interaction respectively. The α and β are t he element types of atom i and j. We use the EAM-alloy potential because we also performed comparable simulations for Cu and Ag–Cu systems. Using the same potential ensures consistent comparison and minimizes artifacts introduced by the choice of interatomic potential. The interaction of carbon atoms in the CNT can be described by the AIREBO potential [38], and can be expressed by:

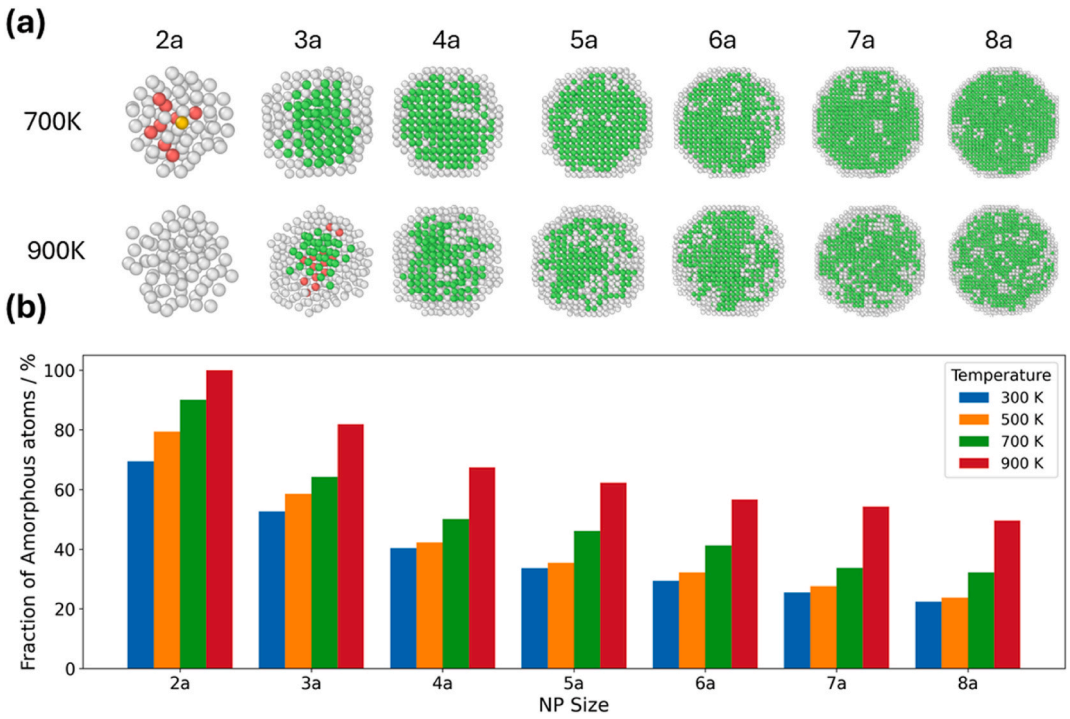

Fig. 1. (a) Snapshots of 2a–8a NP equilibrium structure at 700, and 900 K (green: FCC; red: HCP/stacking faults; white: amorphous/disordered). (b) Amorphous-atom fraction versus NP size and temperature.

$$E = \frac{1}{2}\sum_{i}\sum_{j\neq i}\left[E_{ij}^{\mathrm{REBO}} + E_{ij}^{\mathrm{LJ}} + \sum_{k\neq i,j}\sum_{l\neq i,j,k} E_{kijl}^{\mathrm{TORSION}}\right] \tag{2}$$

In an AIREBO-type form, the total energy E is the sum of short-range covalent (REBO), long-range dispersion (LJ), and dihedral torsion terms; the $1/2$ factor avoids double counting of pairs. The REBO part describes environment-dependent covalent bonds and allows bond making/breaking. The LJ part adds non-bonded van der Waals forces and is suppressed for bonded neighbors. The torsion term penalizes dihedral rotations and helps keep π-conjugation in sp^2 carbon. The L-J potential was used to describe the interaction between Ag and carbon atoms. The LJ parameters, $\varepsilon = 0.0301$eV $\sigma = 3.006$ Å are based on Parnian Yousefi [39]. The NVT ensemble was utilized during the whole simulation process. The timestep was set to 1fs. All the simulations were conducted by LAMMPS [40]. OVITO [41] and Python were used for model visualization and some post-processing.

3. Results and discussion

3.1. Melting simulation

Bulk Ag melts at 1234 K (961 °C), whereas Ag NPs melt at substantially lower temperatures due to finite-size effects. We therefore determine size-dependent NP melting temperatures to interpret the temperature-dependent NP-CNT contact behaviors discussed in Sections 3.2–3.7. In this part, the potential energy (PE) evolution and Lindemann index (LI) evolution with temperature curves can determine the melting points by finding their turning points on the curves. Here, LI is a dimensionless atomic-scale measure of thermal displacement fluctuations that is widely used to indicate lattice instability or melting-like behavior. The equation of LI of system and the LI for each atom can be shown as follow:

$$\delta_{LI,i} = \frac{1}{N-1}\sum_{j\neq i}\frac{\sqrt{\langle r_{ij}^2\rangle - \langle r_{ij}\rangle^2}}{\langle r_{ij}\rangle} \tag{3}$$

$$\delta_{LI} = \frac{1}{N}\sum_{i}\delta_{LI,i} \tag{4}$$

where $\delta_{LI,i}$ is the local Lindemann index of atom i, N is the number of atoms in the selected set, r_{ij} is the instantaneous distance between atoms i and j ($j \neq i$), and $\langle r_{ij}\rangle$ and $\langle r_{ij}^2\rangle$ denote the time-averaged first and second moments over the sampling window. Most of the works mainly used these two values to study the thermal stability of nanostructure [42,43]. Although there are some works have [35,44] already calculated the NP with small size, they were not covered all the situation that NP used in my woks. The resulting values for radii 2a–8a are summarized in Table 1, while the full PE–T and LI–T curves are provided in Fig. S1.

PE- and LI-based melting points show a systematic offset of ~20 K. This discrepancy is expected for finite clusters because LI is more sensitive to the onset of local disorder especially for surface premelting, whereas PE reflects the global energetic transition and can appear slightly later. In the subsequent interfacial analyses we primarily reference the LI-based melting temperature in the discussion of high-temperature activation and transient melting.

The critical value of LI is not universal for finite NPs and varies with size, which marks the onset of melting-like disorder, i.e., when atomic thermal fluctuations become large enough to destabilize the crystalline lattice. Here it is defined in a size-specific manner as the LI value at the LI evolution inflection point for each NP size. It is used only as an internal indicator to classify solid-like versus strongly disordered states at the simulation temperatures. The LI of atoms for each NPs are shown in S2.

Fig. 1 mainly shows equilibrium structures of 2a–8a NPs at high temperature (snapshots at 300 and 500K are in S3) together with the amorphous-atom fraction. At 300 K all sizes remain crystalline and LI values stay well below the size-specific critical LI. At 500 K noticeable surface disorder appears only for the smallest NPs, while larger NPs remain largely ordered. At 700–900 K disorder increases rapidly for small sizes, and transient melting becomes possible for the smallest NPs at 900 K. These baseline trends provide the reference needed to interpret high-temperature interfacial restructuring, energy release, and contact

Table 1
The melting points for NP size from 2a to 8a determined by PE and LI method and their critical LI.

NP size	2a	3a	4a	5a	6a	7a	8a
Melting Points (PE)	800K	940K	1040K	1100K	1140K	1160K	1180K
Melting Points (LI)	780K	920K	1020K	1080K	1120K	1140K	1160K
Critical LI	0.105	0.087	0.076	0.063	0.058	0.050	0.044

evolution in the NP–CNT simulations.

3.2. Comparation between NP-NP and NP-CNT contact behavior

In order to clarify the difference between nanoparticle sintering and nanoparticle–CNT contact, we first compare an Ag NP–NP sintering model with an Ag NP–CNT sidewall contact model under comparable conditions. This comparison is used as a reference for the following analyses on temperature and NP size effects. In our interaction model, the NP–NP system is governed by metallic bonding described by the EAM potential for Ag–Ag interactions. In contrast, the Ag–C cross interaction is described by a non-reactive Lennard–Jones (12–6) potential and no Ag–C chemical bonding, charge transfer, or bond-order/reactive terms are included. Therefore, the interfacial attraction and the group-to-group force in the NP–CNT case originate from the van der Waals-type Ag–C interaction by construction.

It should be noted that the NP–NP and NP–CNT models contain different numbers of atoms. Therefore, the absolute value of total potential energy cannot be directly compared between the two models. In this work, we use the potential energy change (ΔPE) relative to the initial state for each model. In addition, we calculate the group-to-group interaction force between the two contacting parts to directly describe the interaction intensity during the contact process.

Fig. 2(a) shows the PE evolution during the contact process. For the NP–NP system, the PE decreases significantly and rapidly after contact, indicating a strong thermodynamic driving force. This is mainly related to metallic bonding formation and interfacial atomic diffusion, which can promote neck formation and growth during sintering. For the NP–CNT system, the potential energy decrease is much smaller, which means the thermodynamic driving force is obviously weaker than that in NP–NP sintering. This result indicates that NP–CNT contact is not a typical sintering process.

Fig. 2(b) shows the group-to-group interaction force. For the NP–NP system, the interaction force increases sharply after contact and keeps at a relatively high level for a period of time, which is consistent with the strong interfacial attraction and continuous atomic rearrangement in sintering. For the NP–CNT system, the interaction force is much lower and decays faster after the initial contact. This is expected because the only cross interaction between Ag and CNT carbon atoms in our model is the 12–6 Lennard–Jones potential; hence the NP–CNT group-to-group

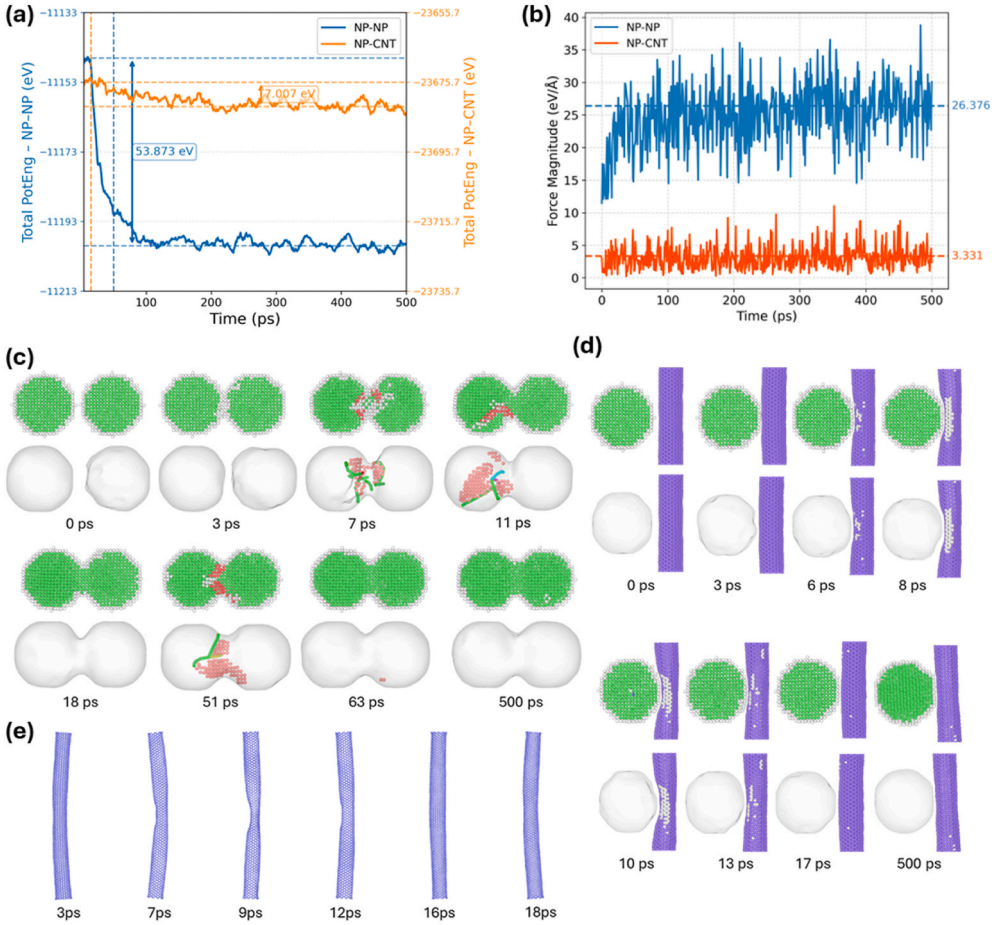

Fig. 2. (a) Total PE evolution for NP–NP (blue, left axis) and NP–CNT (orange, right axis). (b) Force magnitude evolution for NP–NP (blue) and NP–CNT (orange). (c) and (d) are the snapshots of NP-NP system and NP-CNT system respectively. For each panel, the top image is the cross session of model and the bottom image is the surface mesh with HCP atoms and dislocation. (e) CNT bending profiles during NP–CNT contact evolution.

force directly reflects van der Waals-type interaction without any diffusion-driven metallic neck growth.

Fig. 2(c) and (d) further present the snapshot sequences of the NP–NP and NP–CNT systems, respectively. For NP–NP (Fig. 3(c)), the two particles first contact at about 3 ps and an amorphous interfacial layer forms. By 7 ps, dislocations and stacking faults nucleate in the neck region, accompanied by local structural transformation (amorphous → HCP → FCC), and this first restructuring stage is basically finished by ~11 ps. With dislocation glide, the related stacking faults move into the NP, and by ~18 ps, dislocations can be emitted to the free surface, while most amorphous/HCP atoms in the bulk retransform back to FCC. After a short quasi-equilibrium period, a second episode occurs due to the residual surface-energy driving force: at ~51 ps the neck thickens and new stacking faults/dislocations form again, and by ~63 ps this second episode is nearly completed. No further obvious structural transition is observed up to 500 ps, showing a crystalline–amorphization–recrystallization pathway during NP–NP coalescence.

By contrast, for NP–CNT (Fig. 3(d)), the NP touches the CNT at about 3 ps. By ~6 ps, it induces an elastic indentation of the CNT, which peaks around ~8 ps and then gradually recovers by ~17 ps. After that, the interfacial carbon atoms exhibit damped quasi-harmonic oscillations. During the whole process, no clear defect nucleation is observed in the NP bulk. The NP can slightly wander on the CNT under thermal fluctuations, and only a limited interfacial expansion of Ag atoms is observed, indicating relatively poor wetting under this condition.

Fig. 2(e) further shows the global bending behavior of the CNT during the early-stage contact process in the NP–CNT model (500 K, 5a NP). After the first touch (~3 ps), the CNT undergoes a bending deformation, and the curvature increases with time. A larger bending is observed around 7–12 ps, corresponding to the period when the NP keeps pressing the CNT wall and local indentation develops. After that, the CNT gradually rebounds, and the tube shape becomes closer to the initial straight configuration at ~16–18 ps, indicating an elastic recovery with damping. This bending response suggests that, under this condition, the NP–CNT contact is mainly accommodated by CNT elastic deformation rather than by defect nucleation or lattice-scale reconstruction inside the Ag NP, which is consistent with the much weaker ΔPE and interaction force shown in Fig. 2(a and b).

The above results show that the NP–CNT system has a much weaker driving force compared with the NP–NP sintering system. Mechanistically, NP–NP sintering is dominated by metallic bonding and diffusion at the interface, which can drive obviously lattice-scale reconstruction in the neck region together with repeated amorphization–recrystallization. In contrast, NP–CNT contact is mainly controlled by adsorption interaction and geometry-related accommodation. As shown in Fig. 3(d and e), the main response of the NP–CNT model under 500 K is CNT deformation and only limited interfacial adjustment of Ag atoms, while no obvious defect nucleation is observed in the Ag NP bulk. Therefore, in the following sections, we focus on how temperature and NP size can further activate local rearrangement in the NP–CNT system.

3.3. Temperature effect

In this section, we fix the NP size (5a) to isolate the temperature effect on NP–CNT contact behavior. The simulations are performed at 300, 500, 700, and 900 K. It should be noted that at high temperatures, some quantitative values may become more sensitive to the Ag–C Lennard-Jones parameters and cutoff settings. Therefore, we mainly focus on robust trends with temperature.

Fig. 3 shows the evolution of the system total PE at different temperatures. Since the atom numbers are fixed in this section, we still use the total PE and ΔPE relative to the initial state for consistency with previous analyses. At 300 K, the net PE change is close to zero, indicating that the system is mainly governed by thermal vibration and weak adsorption, and it reaches a steady state quickly. At 500 K, the PE decreases slightly with a net drop of ~10.5 eV, and the system stabilizes within a relatively short time. When temperature increases to 700 K, the PE decrease becomes significantly larger (~53.8 eV), while the overall relaxation time is still comparable to that at 500 K. At 900 K, the PE drop becomes much larger (about ~240 eV), and a clear multi-stage relaxation behavior is observed. The PE decreases slowly first, then drops rapidly at late time (around ~300 ps within ~30–50 ps), and finally approaches a plateau, indicating a temperature-activated late-time structural adjustment at the interface.

3.3.1. Early stage contact cycle

After the NP approaches the CNT within the interaction cutoff, the system shows a quasi-periodic compression–rebound motion after the first contact. Fig. 4(a) presents the time-sequenced snapshots from 0 to 20 ps for each temperature, and the corresponding short-time CNT deviation traces are shown underneath. Here, the deviation is defined as the displacement of interfacial carbon atoms relative to their pristine positions; negative values indicate inward indentation toward the NP, while positive values indicate outward bulging.

At 300 K, the NP touches the CNT at about ~3 ps. After contact, the NP continues moving toward the CNT and compresses the tube wall, and the indentation increases until reaching a maximum (around ~7–9 ps). During this process, some carbon atoms near the interface become locally disordered due to strong local deformation. After that, the CNT starts to rebound, and the indentation gradually decreases. Around

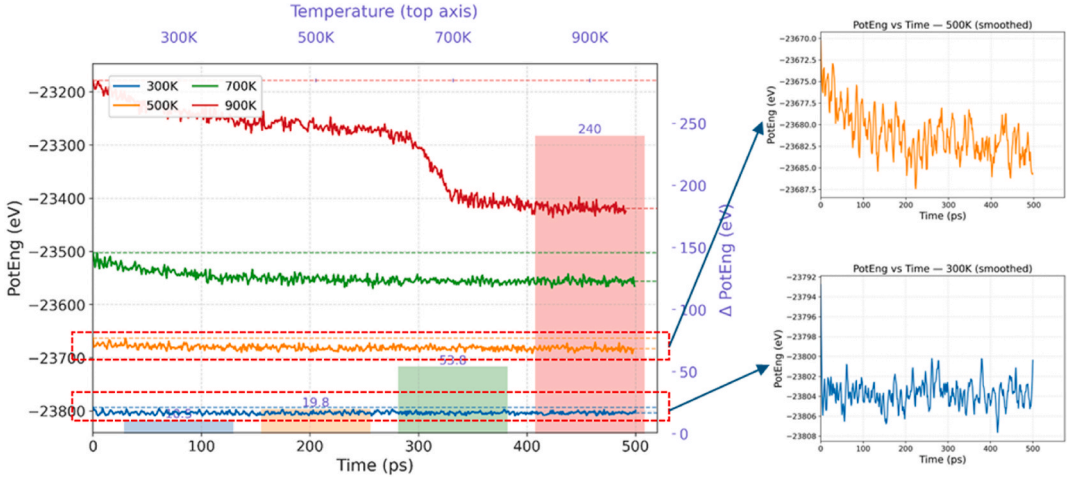

Fig. 3. NP–CNT system with NP radius 5 nm. Total PE versus time at 300, 500, 700, and 900 K; shaded regions and dashed lines indicate the ranges/reference levels used to compute change value of PE.

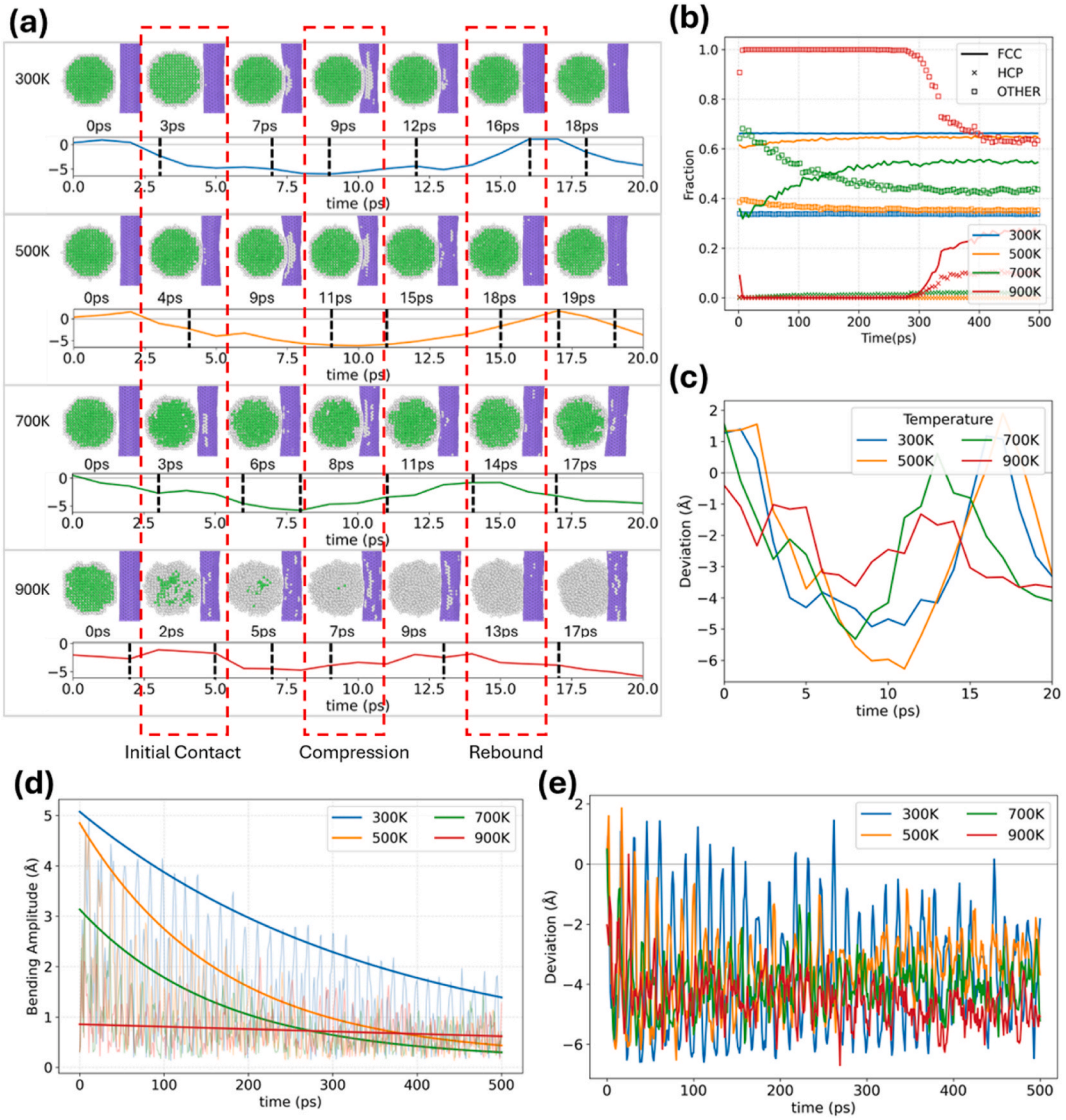

Fig. 4. NP–CNT bonding at 300, 500, 700, and 900 K (5a NP). (a) Time-sequenced snapshots from 0 to 20 ps with the corresponding short-time CNT deviation traces; red dashed boxes mark the selected frames. (b) Schematic CNT profiles. (c) Phase fractions (FCC/HCP/OTHER) versus time. (d) Early-time interfacial deviation (0–20 ps). (e) Bending amplitude versus time (0–500 ps). (f) Long-time deviation versus time (0–500 ps). Color scheme as in the previous snapshots.

16–18 ps, the first compression–rebound cycle is basically completed, and the system enters the next oscillation cycle.

With increasing temperature, the early-stage contact cycle becomes weaker. At 500 K, the contact sequence is similar to that at 300 K, but the indentation amplitude is smaller and the rebound occurs earlier. At 700 K and 900 K, the compression–rebound motion is further suppressed, and the short-time deviation amplitude becomes smaller, indicating that temperature promotes faster local accommodation and damping at the interface.

Fig. 4(b)tracks NP phase fractions over the whole simulation and shows that the particle remains predominantly FCC at 300–700 K, with only small, cycle-induced fluctuations in HCP and disordered atoms; within the first 0–20 ps the changes are negligible. At 900 K, however, a late-time rearrangement appears, where the FCC fraction drops and the disordered fraction rises indicating temperature-activated restructuring beyond the initial elastic cycle.

Fig. 4(c) shows the short-time interfacial deviation in the first compression–rebound cycle after the initial touch. At all temperatures, the CNT wall is first pushed inward (negative deviation) and reaches a minimum at ~8–10 ps, followed by a rebound toward a less negative level at ~15–18 ps, reflecting an underdamped early-stage press–release response. The indentation amplitude decreases with temperature. The minimum deviation is typically ~−5 to −6 Å at 300–700 K, but becomes much smaller at 900 K with a weaker rebound. This indicates that higher temperature suppresses coherent elastic oscillation.

3.3.2. *Long-time deformation*

Fig. 4(d) shows the time evolution of the global bending amplitude up to 500 ps. The initial bending amplitude follows the order of 300 K > 500 K > 700 K > 900 K, while the damping rate shows the opposite order (fastest decay at 900 K and slowest at 300 K). All curves present a two-stage decay behavior. A fast drop in the early stage followed by a slower relaxation. By the end of simulation, the amplitudes converge to a low-level range, and the 300 K case still keeps a slightly larger residual bending.

Fig. 4(e) is the local interfacial deviation over 0–500 ps. Although the signal is noisier than the global bending trace, it remains periodic and oscillates around a negative offset (typically between −3 and −5 Å), indicating a persistent inward bias at the contact wall. The temperature dependence is consistent with bending. 300 K shows the largest oscillation amplitude and slowest decay, while 900 K shows the smallest oscillation amplitude and fastest convergence. This indicates that

increasing temperature suppresses both global bending and local indentation, and also accelerates damping, which is consistent with more active interfacial relaxation at higher temperatures.

3.3.3. Interface evolution and stress response

Fig. 5 summarizes the interfacial geometry and CNT stress state at different temperatures (two representative frames in compression and rebound stages). Interfacial atoms are identified by a hetero-coordination criterion: for each carbon atom, Ag neighbors within a cutoff are counted, and atoms with at least one unlike neighbor are labeled as interfacial; the cutoff used here is 4 Å.

From Fig. 5(a and b), the interfacial atoms are mainly distributed along the tube axis, meaning the contact is relatively long in the axial direction but short in the circumferential direction. During compression, the number of interfacial atoms increase and the contact surface becomes more curved, corresponding to a larger effective interfacial area. During rebound, the interfacial atom count decreases and the interface becomes nearly planar. With temperature increasing from 300 K to 900 K, the interfacial atom count generally increases and the distribution becomes broader. At 900 K, the difference between compression and rebound becomes smaller, suggesting a more persistent contact at high temperature.

Fig. 5(c) shows the CNT von Mises stress maps. The stress is evaluated based on LAMMPS stress/atom outputs combined with per-atom Voronoi volumes to recover the stress tensor. In general, during compression, stress concentrates on both sides of the contact band, while during rebound, the hotspot shifts closer to the interface and the average stress is smaller. With temperature increasing, the mean stress level at 300–500 K is higher than that at 700–900 K, indicating that higher temperature can reduce peak stress by promoting local relaxation. However, at high temperature the number of atoms in the high-stress range becomes larger, and the stress patterns in compression and rebound stages become more similar, implying that the interfacial deformation becomes more distributed rather than highly localized.

3.4. Size effect

In this section, we investigate how NP size affects NP–CNT contact behaviors across the same temperature set. The NP radius varies from 3a to 8a. Since the CNT geometry is fixed, changing NP size simultaneously changes the local curvature mismatch, the effective contact width/area, and the NP surface-to-volume ratio. Therefore, size effects are expected not only in energetics but also in CNT deformation, interfacial stress distribution, and NP structural evolution.

Fig. 6(a) shows the time evolution of PE for NP sizes 3a–8a at 300, 500, 700, and 900 K, and Fig. 6(b) summarizes the corresponding PE change ΔPE. At 300 K, all sizes exhibit nearly flat PE traces over 0–500 ps with only minor thermal fluctuations, indicating negligible structural rearrangement. At 500 K, only the 3a NP shows a noticeable initial PE drop, whereas larger particles remain close to horizontal. At 700 K, all sizes show a clear PE decrease, suggesting thermally activated interfacial accommodation. In this regime, the 3a NP shows the largest ΔPE and the longest time to approach a quasi-steady state, while for 4a–8a the relaxation time generally increases with size. At 900 K, the PE reduction becomes strongly size-dependent: 3a drops rapidly and then tails off slowly; 4a–5a show an apparent multi-stage behavior with an intermediate plateau; and 6a–8a relax more slowly overall.

From Fig. 6(b), ΔPE increases significantly with temperature for all sizes, while the size corresponding to the maximum ΔPE shows a temperature dependence. This is reasonable because ΔPE is controlled by both the available surface energy, which is more pronounced for small NPs due to high surface-to-volume ratio and the real contact area which usually increases with NP size. Therefore, the ΔPE trend reflects a competition between “surface-energy density” and “contact-area scale”, rather than a simple monotonic size dependence.

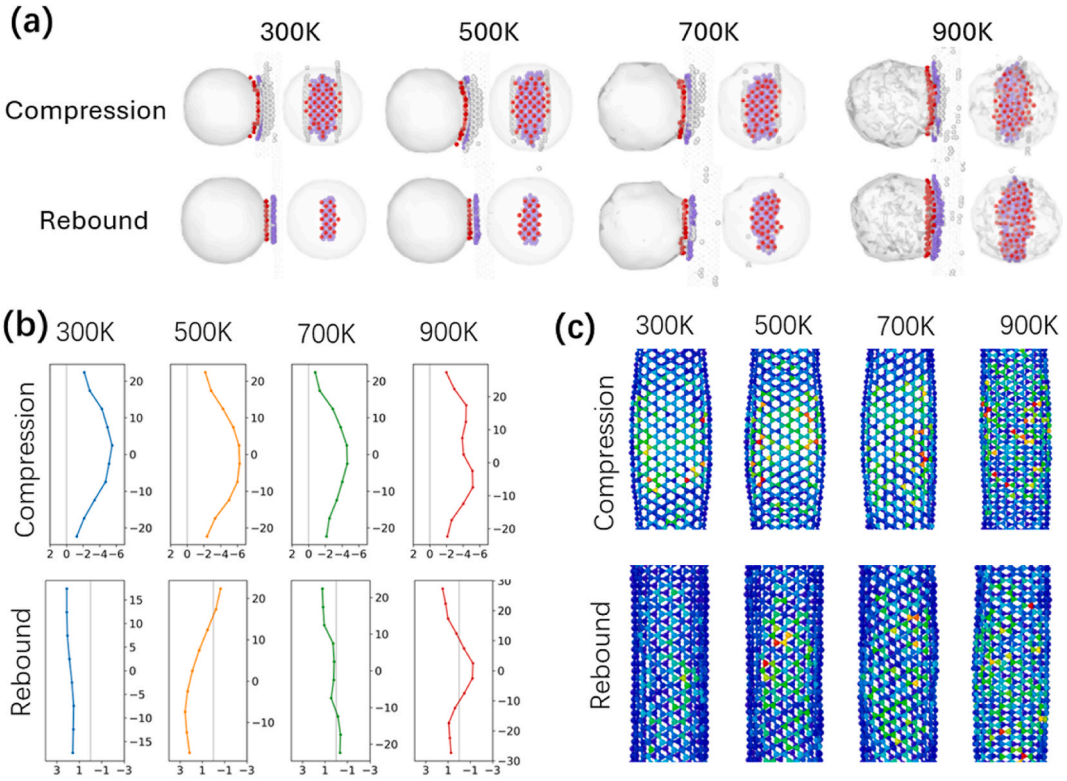

Fig. 5. Interface characterization during the first NP–CNT cycle at 300, 500, 700, and 900 K. (a) Bonding configurations with smoothed NP/CNT surfaces; interfacial atoms highlighted. (b) Axial segmentation and center-line fits of the CNT wall for the same frames. (c) CNT von Mises stress maps computed from LAMMPS stress/atom combined with per-atom Voronoi volumes.

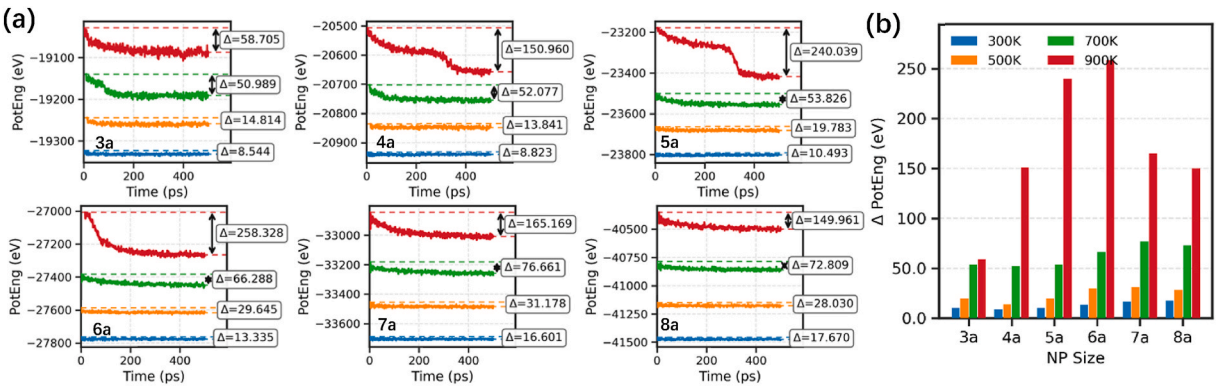

Fig. 6. Potential-energy (PE) evolution versus time for NP–CNT contact across NP sizes 3a–8a at 300, 500, 700, and 900 K. (a) Time-series PE curves for each size. (b) Summary bar chart of ΔPE as a function of NP size for each temperature.

3.4.1. *CNT deformation: bending and indentation versus size*

To directly describe CNT mechanical response, we quantify both global bending and local indentation/deviation as a function of NP size and temperature. Fig. 7(a) summarizes the maximum CNT bending amplitude. Overall, the maximum bending increases nearly linearly from 3a to 8a, indicating that larger NPs induce stronger global deformation of the CNT. Meanwhile, increasing temperature suppresses the bending amplitude and enhances damping, consistent with faster interfacial relaxation at higher temperatures. In addition, distinct relaxation drops are still observed for specific size–temperature combinations indicating a size-dependent activation temperature for efficient dissipation of CNT bending strain energy.

Fig. 7(b) reports the mean-square interfacial deviation. The deviation magnitude generally increases with NP size but decreases with temperature, consistent with the bending trend. In particular for each size, the deviation shows a threshold-like reduction at a characteristic temperature range, suggesting that once thermally activated interfacial accommodation becomes effective, both bending and indentation are reduced simultaneously.

3.4.2. *Interfacial stress: layer-resolved distribution and size dependence*

Fig. 8 presents the layer-resolved von Mises stress near the NP–CNT contact. Layers are defined along the local surface normal direction, with layer 0 at the geometric boundary, negative layers toward the interior, and positive layers toward the exterior. For each case, the layer-averaged stress is reported.

Across most conditions, the maximum stress occurs at layer −1, indicating a subsurface stress concentration directly beneath the contact region. At 700 K, the peak shifts inward to layer −2 for some cases, and inner-layer stresses become more uniform, consistent with deeper stress penetration under stronger thermally activated accommodation. In the lower-temperature regime (300–500 K), interfacial stress generally increases with NP size, which is consistent with the larger contact area and stronger geometric constraint induced by larger NPs. At 700 K, stress becomes more distributed through the subsurface layers and the maximum may shift inward. At 900 K, the maximum interfacial stress tends to decrease with NP size, suggesting that large NPs at high temperature can relax stress concentration more effectively, leading to a lower peak stress level.

The stress peak is generally subsurface (layer −1/−2), implying that CNT damage risk is mainly controlled by subsurface concentration rather than the outermost surface layer. Size tends to increase peak stress at low temperatures (stronger constraint), while at high temperature stress concentration is reduced, especially for larger NPs due to enhanced relaxation.

3.4.3. *Size-dependent structural evolution of the NP during contact*

Fig. 9(a–d) shows the time evolution of FCC/HCP/Other fractions for NP sizes 3a–8a at different temperatures, and Fig. 9(e) provides representative cross-sectional snapshots. At 300 K, phase fractions remain nearly constant for all sizes, indicating negligible structural evolution. At 500 K, only the 3a NP exhibits a small adjustment before reaching a plateau. At 700 K, smaller sizes (3a–5a) show a decrease of amorphous structure and an increase of crystalline fractions within ~0–200 ps, whereas larger sizes evolve more slowly. At 900 K, all sizes exhibit stronger restructuring, and the time required to reach a steady state generally increases with particle size.

The snapshots indicate a shared pathway for most sizes except for the smallest NP under strong activation. The NP first becomes more disordered near the interface and then recrystallizes, and the recrystallization tends to initiate from the CNT-contacting region followed by growth toward the interior. During this process, HCP may appear transiently (4a–6a), which can be interpreted as stacking-fault/twinning-related intermediates and then converts to FCC. For the smallest NP (e.g., 3a) at high temperatures, the NP can become highly disordered and the structural identification of FCC/HCP becomes less stable, which is consistent with its high surface activity observed in the melting baseline. Therefore, increasing temperature promotes interface-assisted rearrangement and recrystallization, while increasing size raises the activation threshold and slows down the overall structural evolution. Smaller NPs are more prone to strong disordering and faster transitions due to their higher surface activity.

Combining Figs. 6–9, NP size affects NP–CNT contact through coupled energetic–mechanical–structural pathways. Larger NPs induce stronger CNT deformation and can increase subsurface stress concentration at low temperatures, while smaller NPs show higher surface activity and stronger thermally activated rearrangement at elevated temperatures. Temperature amplifies ΔPE for all sizes but also accelerates deformation damping and reduces stress localization. These size–temperature coupled trends provide a quantitative basis for selecting NP size under different processing temperature windows.

3.5. *Mechanism of transient melting and recrystallization at 900 K*

As discussed in Section 3.3, the 900 K NP–CNT case shows a clear multi-stage PE relaxation rather than a single monotonic decay. For clarity, we align the structural evolution with the PE segments and summarize the pathway as four stages: Stage I is initial contact and fast accommodation, Stage II is a long quasi-steady period with limited net relaxation), Stage III is a late-time rapid PE drop around ~290–340 ps, and Stage IV is post-transition slow relaxation toward a plateau. Importantly, the sharp PE decrease in Stage III coincides with a pronounced structural transition, indicating that the late-time relaxation is not simply thermal damping of CNT deformation but is associated with internal reordering of the Ag NP.

The structural-fraction evolution provides a direct signature of this

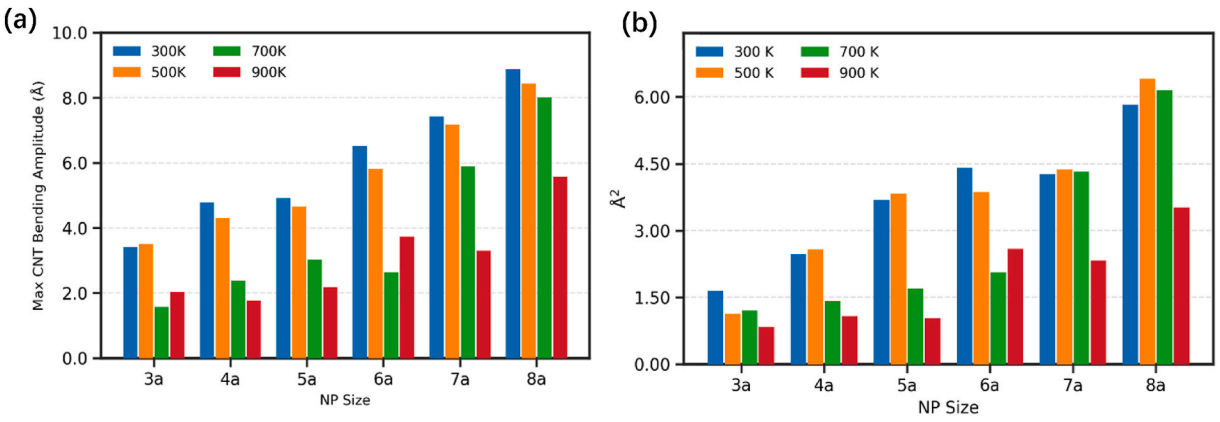

Fig. 7. (a) Grouped bar chart of the maximum CNT bending amplitude for NP sizes 3a–8a at 300, 500, 700, and 900 K. (b) Companion statistic summarizing the mean-square interfacial deviation (Å^2) over the full trajectory for the same cases.

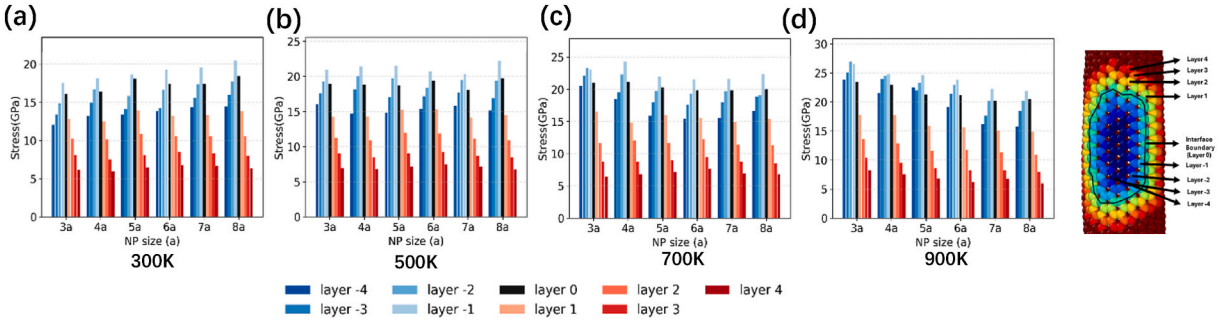

Fig. 8. Layer-resolved interfacial stress near the NP–CNT contact. (a–d) Bar charts of von Mises stress for layers −4 … +4 at 300 K, 500 K, 700 K, 900 K (left to right) across NP sizes 3a–8a. Layers are defined along the surface normal with 0 at the boundary, negatives inside and positives outside.

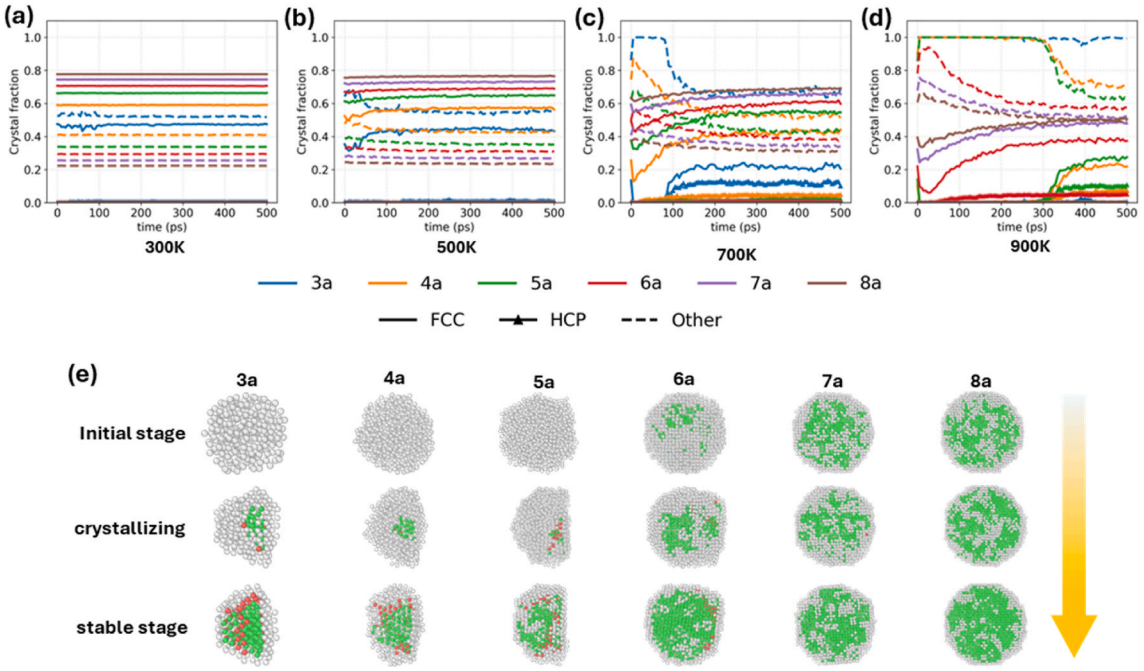

Fig. 9. Size–temperature dependence of NP crystallinity. (a–d): time evolution (0–500 ps) of crystal fractions for NP sizes 3a to 8a at 300 K, 500 K, 700 K, and 900 K, respectively (curves grouped by NP size). (e) is corresponding cross-section snapshots.

transition. During Stages I–II, the NP remains largely disordered in the interfacial/near-surface region, consistent with a transiently amorphized state at elevated temperature. Once entering Stage III, the amorphous structure fraction drops rapidly while FCC/HCP fractions increase, demonstrating an amorphous-to-crystalline transformation. After ~340 ps (Stage IV), the major transformation is essentially

completed, and only slow coarsening/adjustment continues, consistent with the PE approaching a plateau.

To visualize the crystallization more clearly, Fig. 10(a) shows cross-sectional snapshots of the bonding structure, with the corresponding nucleation morphologies displayed beneath each snapshot (reoriented viewing direction to reveal internal grain relationships). At the onset of Stage III (~290 ps), a small crystalline embryo appears from the amorphous matrix near the NP–CNT interface. This embryo is only marginally stable at first but serves as a seed for subsequent growth. The crystalline region then expands outward from the interface-adjacent site into the NP bulk, accompanied by stacking-fault formation; by ~340 ps, the main amorphous-to-crystalline transformation is basically finished, leaving a multi-grain NP separated by stacking faults.

The fact that nucleation is observed near the interface is physically reasonable for two reasons. First, an interface generally reduces the nucleation barrier by providing a site that partially replaces the high-energy nucleus surface. Second, the NP–CNT contact region is where local structural frustration and atomic mobility are highest at 900 K, which induce interface has disordering or premelting tendency. It naturally becomes the most probable location for a stable embryo to form once the system enters the late-time relaxation window.

To verify whether twin boundaries formed after the 900 K recrystallization event, we performed grain segmentation using the Polyhedral Template Matching (PTM) method in OVITO and quantified grain-to-grain misorientations using the quaternion-based orientation analysis (details are provided in the Supplementary Materials). At the end of the simulation, the NP is partitioned into multiple grains, and the misorientation analysis indicates that the dominant grain (G1) forms Σ3{111} twin relationships with several neighboring grains (G2, G3, G5, and G6), whereas other grain pairs do not satisfy the Σ3 criterion. These results confirm that the final state corresponds to a multiply twinned structure. Mechanistically, the emergence of Σ3{111} twins is consistent with a stacking-fault-mediated recrystallization pathway during rapid ordering in FCC metals, in line with the stacking faults observed during grain expansion and the interface-adjacent nucleation in Stage III.

Overall, in the 900 K NP–CNT case, the sharp Stage-III PE drop is directly tied to an amorphous to crystalline structure evolution recovery initiated near the interface, followed by slow relaxation. The interface-adjacent nucleation and the resulting multiply twinned structure which is dominated by Σ3{111} together indicate an interface-mediated recrystallization route that can be activated in NP–CNT contact under high temperature even with relatively weak overall driving force.

3.6. Solid-state wetting

The NP–CNT system studied here is a solid–solid contact, rather than a classical liquid droplet. In solid-state wetting, the apparent contact geometry is governed not only by interface/surface energetics, but also by elastic strain energy, anisotropy/surface stiffness, and the physics localized near the triple-line/edge, while the morphological adjustment is typically mediated by surface diffusion instead of hydrodynamic flow. Therefore, we use "wetting angles" as an effective geometric descriptor of interfacial accommodation to compare different temperatures, NP sizes, and CNT directions, without implying a liquid-like spreading mechanism.

We define a local (intrinsic) contact angle on the local tangent plane of the CNT at the true contact line, and convert it to a normalized accommodation/adhesion index,

$$W^* \equiv 1 + \cos\theta^l \tag{5}$$

which serves as an effective measure of how efficiently the NP conforms to the CNT surface under a given condition. Because the CNT is curved and deformable, we also distinguish θ^l from an ideal reference angle θ^i to quantify indentation- or wrapping-induced tangent rotation (schematic in Fig. 11(d and e)). The detailed energetic framework and solid-state corrections (anisotropy, line/edge terms) are provided in the Supplementary Information.

Fig. 11(a) summarizes W^* versus NP size along the axial direction. Overall, W^* decreases with increasing NP size, indicating that smaller NPs exhibit stronger solid-state accommodation on the CNT. The temperature dependence is most pronounced for small NPs (≈3–5a), where elevated temperature increases W^*, consistent with enhanced interfacial atomic rearrangement and a larger indentation-induced tangent rotation. For larger NPs (≳6a), the curves converge, implying that axial accommodation becomes increasingly limited by geometry and the CNT's global stiffness rather than by thermal activation alone.

In the circumferential direction which is shown in Fig. 11(b), W^* also decreases with NP size, but the sensitivity collapses faster with size (typically by ~ 5a). This behavior reflects the dominance of cylindrical curvature and the onset of partial wrapping. Small NPs at elevated temperature can develop a more conformal rim contact, whereas larger NPs remain curvature-limited and show weak temperature sensitivity. The contrast between axial and circumferential trends highlights that axial W^* is primarily controlled by indentation–bending coupling, while circumferential W^* is governed by curvature-constrained conformity.

To connect geometry to energetics, we further evaluate the fraction of the total energy drop that can be attributed to effective interfacial accommodation,

$$\chi_{\mathrm{wet}} \equiv \Delta E_{\mathrm{wet}} / \Delta E_{\mathrm{tot}} \tag{6}$$

where ΔE_{wet} is estimated from W^* and the time-averaged contact area. Fig. 11(c) shows that χ_{wet} generally decreases with increasing NP size and temperature, suggesting a transition from adhesion-dominated relaxation to non-wetting-dominated relaxation, where contributions from NP surface relaxation, local structural rearrangement, and CNT elastic accommodation become increasingly important.

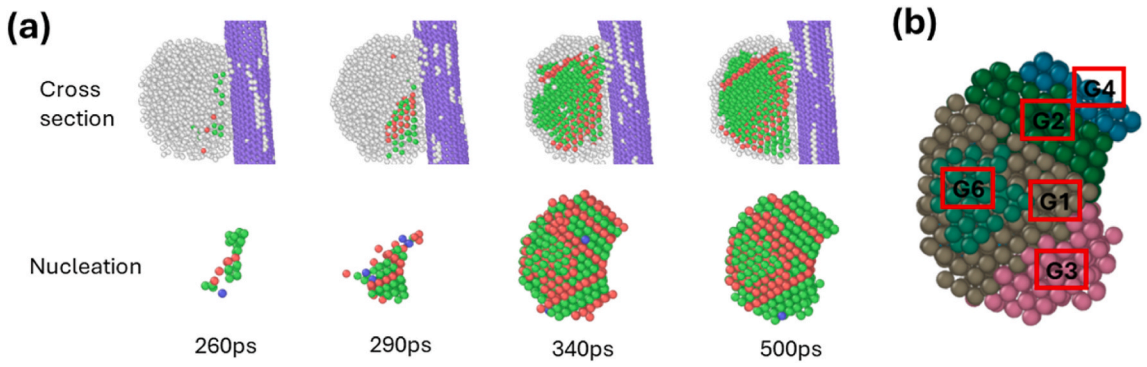

Fig. 10. (a) Crystallization pathway of the NP at 900 K during NP–CNT contact. Top row is cross-sectional snapshots (CNT in purple) from nucleation to growth and bottom row is corresponding "nucleation views" of the same frames. (b) final grain map with representative grains labeled G1–G6 (G5 located on the back side).

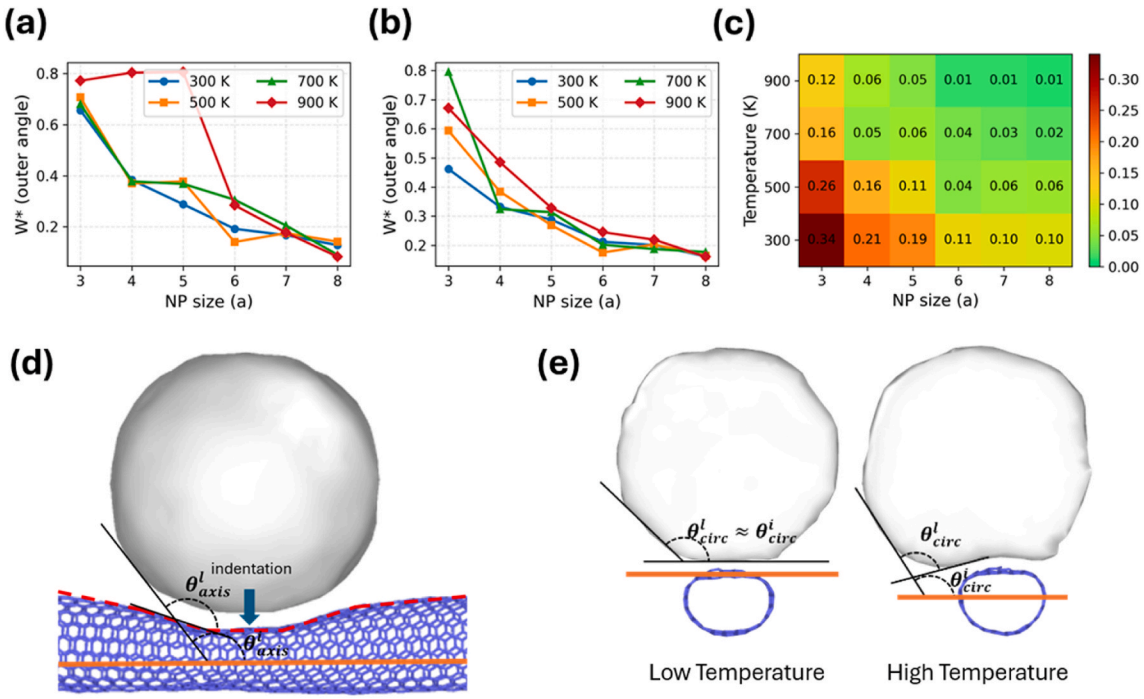

Fig. 11. Normalized adhesion $\boldsymbol{W}^*$ vs NP size along the axial direction at 300/500/700/900 K. (b) $\boldsymbol{W}^*$ vs size in the circumferential direction. (c) Heatmap of the wetting share $\chi_{\mathbf{wet}} = \boldsymbol{W}^*/\varphi_c$ (warmer = larger wetting contribution). (d) Axial schematic. (e) Circumferential schematic.

Finally, Fig. 11(d and e) illustrates why θ^l can deviate from θ^i. In the axial section, indentation rotates the local tangent and yields $\Delta\theta_{\mathrm{ax}} = \theta^l_{\mathrm{ax}} - \theta^i_{\mathrm{ax}}$, which increases with indentation depth and local curvature. In the circumferential section, partial wrapping produces an analogous rotation $\Delta\theta_{\mathrm{circ}}$ controlled by the wrap angle. These differences are primarily geometric–elastic consequences of solid-state accommodation, rather than signatures of liquid-like spreading.

Overall, the effective adhesion index W^* decreases with NP size in both directions, indicating that smaller NPs conform more efficiently to the CNT surface, while the axial response remains more temperature-sensitive due to indentation–bending coupling and the circumferential response becomes curvature-limited at larger sizes. Meanwhile, the wetting share χ_{wet} drops with increasing size and temperature, implying that relaxation progressively shifts from adhesion-controlled accommodation to non-wetting contributions. The observed $\theta^l - \theta^i$ gap is best interpreted as a geometric–elastic tangent-rotation effect in solid–solid contact rather than liquid-like spreading.

3.7. Design implications for CNT–metal nanoparticle interconnections

The above results show that NP–CNT contact is controlled by NP size, temperature, and the CNT curvature direction. Smaller NPs usually show stronger accommodation on the CNT surface. Increasing temperature can further enhance this trend, because higher temperature promotes interfacial rearrangement and makes the NP easier to conform to the CNT. However, high temperature is not always better. At high temperature and small NP size, the NP can undergo a transient disordering and then recrystallize. This process can produce multiple grains and extensive twinning. Therefore, stronger accommodation may come with microstructural reconstruction. If structural stability is more important, a safer process window is larger NPs with low or intermediate temperature. In this window, the contact response is mainly elastic. The NP bulk also remains more stable.

CNT deformation provides another clear guideline. Indentation and bending are coupled. Damping is part of the same response. With increasing temperature, the indentation and bending amplitudes become smaller. The damping also becomes faster. This indicates that more energy is dissipated at the interface. It also helps stabilize the contact geometry. Stress results suggest a trade-off. Higher temperature can reduce the peak stress and increase the number of stressed atoms which lead to stress becoming less localized.

The axial–circumferential difference is also important. Axial accommodation is more sensitive to indentation and bending, which is more temperature dependent. Circumferential accommodation is primarily constrained by the CNT's cylindrical curvature, so it becomes size-dominated more quickly, and clear wrapping effects mainly appear only for small NPs at elevated temperature. As a result, CNT orientation and texture can change wetting strength, deformation mode, and stress distribution in NP–CNT interconnections.

4. Conclusion

The MD results build a mechanism-consistent picture of solid-state Ag NP–CNT contact. We link energetics, structural pathways, CNT mechanical accommodation, stress localization, and curvature-induced anisotropy into one chain. This study distinguishes elastic NP–CNT contact from interface-activated structural evolution, and identifies the conditions that promote the transition.

- The NP–NP pair shows a much stronger driving force. In NP–CNT, the interaction is weaker and relaxes faster. The contact is mainly accommodated by adsorption and CNT deformation, rather than diffusion-driven neck growth and dislocation-mediated coalescence.
- Under high temperature and small NP size, the system can enter a transient melting to recrystallization pathway. The final NP becomes multi-grained. Σ3-type twins are confirmed by grain segmentation and misorientation analysis.
- Indentation, global bending, and damping are not separate effects. They are different expressions of the same accommodation response.
- Interfacial stress concentrates near the contact boundary and into subsurface layers. With increasing temperature, the peak stress is reduced, but a broader region carries moderate stress. This identifies where damage is most likely to initiate in NP–CNT joints.

- Axial and circumferential behaviors are different because CNT curvature limits conformity and rotates the local tangent at the contact line. CNT texture can serve as an effective design parameter to tune adhesion-like metrics and stress distribution in NP–CNT interconnect structures.

Declaration of competing interest

The authors declare that they have no known competing financial interests or personal relationships that could have appeared to influence the work reported in this paper.

Acknowledgement

This work was supported by Special Support Program for Cultivating High-level Talents in Guangdong Province (2023TQ07C475), and the Shenzhen Major Science and Technology Projects (Grant No. KJZD20240903102309013).

Appendix A. Supplementary data

Supplementary data to this article can be found online at https://doi.org/10.1016/j.jmrt.2026.02.194.

References

[1] Jin J, Liu P, Deng Y, Zhang Z. Reliability study of critical structural redistribution layers in advanced packaging: a review. IEEE Trans Reliab 2025;74:3371–82. https://doi.org/10.1109/TR.2025.3556255.
[2] Zhang Y, Dong D, Li Q, Zhang R, Udrea F, Wang H. Wide-bandgap semiconductors and power electronics as pathways to carbon neutrality. Nat Rev Electr Eng 2025;2:155–72. https://doi.org/10.1038/s44287-024-00135-5.
[3] Asim M, Baig T, Siddiqui FR, Khan S, Khan SA, Babar H, Said Z, Zhao J, Abidi IH. Advancements in thermal management solutions for electric vehicle high-power electronics: innovations, cooling methods, and future perspectives. J Energy Storage 2025;111:115344. https://doi.org/10.1016/j.est.2025.115344.
[4] Gao X, Jia Q, Wang Y, Zhang H, Ma L, Zou G, Guo F. Review on power cycling reliability of SiC power device. Electronic Materials 2024;5:80–100. https://doi.org/10.3390/electronicmat5020007.
[5] Gan CL, Huang CY. Materials for thermal management in advanced memory packaging. In: Gan CL, Huang CY, editors. Electronic materials innovations and reliability in advanced memory packaging. Cham: Springer Nature Switzerland; 2025. p. 101–28. https://doi.org/10.1007/978-3-031-94795-7_5.
[6] Saeed IK. Carbon nanotubes?properties and applications: a review. Carbon Lett 2013;14:131–44. https://doi.org/10.5714/CL.2013.14.3.131.
[7] Chen Z, Zhang J, Wang S, Wong C-P. Challenges and prospects for advanced packaging. Fundam Res 2024;4:1455–8. https://doi.org/10.1016/j.fmre.2023.04.014.
[8] Cheng X, Pan Z, Fan C, Wu Z, Ding L, Peng L. Aligned carbon nanotube–based electronics on glass wafer. Sci Adv 2024;10. https://doi.org/10.1126/sciadv.adl1636. eadl1636.
[9] Maheswaran R, Shanmugavel BP. A critical review of the role of carbon nanotubes in the progress of next-generation electronic applications. J Electron Mater 2022;51:2786–800. https://doi.org/10.1007/s11664-022-09516-8.
[10] Zou H, Feng Y, Qiu L. Interfacial heat conduction enhancement mechanism between CNTs encapsulated with LCC. Chem Eng J 2025;523:168842. https://doi.org/10.1016/j.cej.2025.168842.
[11] Ladani L. The potential for metal–carbon nanotubes composites as interconnects. J Electron Mater 2019;48:92–8. https://doi.org/10.1007/s11664-018-6734-3.
[12] Uhlig B, Dhavamani A, Nagy N, Lilienthal K, Liske R, Ramos R, Dijon J, Okuno H, Kalita D, Lee J, Georgiev V, Asenov A, Amoroso S, Wang L, Koenemann F, Gotsmann B, Goncalves G, Chen B, Liang J, Pandey RR, Chen R, Todri-Sanial A. Challenges and progress on carbon nanotube integration for BEOL interconnects. In: 2018 IEEE international interconnect technology conference (IITC); 2018. p. 16–8. https://doi.org/10.1109/IITC.2018.8454842.
[13] Malaki M, Fadaei Tehrani A, Niroumand B, Gupta M. Wettability in metal matrix composites. Metals 2021;11:1034. https://doi.org/10.3390/met11071034.
[14] Chen J, Yan L, Liang S, Cui X, Liu C, Wang B, Zou L. Remarkable improvement of mechanical properties of layered CNTs/Al composites with Cu decorated on CNTs. J Alloys Compd 2022;901:163404. https://doi.org/10.1016/j.jallcom.2021.163404.
[15] Upadhyay G, Saxena KK, Sehgal S, Mohammed KA, Prakash C, Dixit S, Buddhi D. Development of carbon nanotube (CNT)-reinforced Mg alloys: fabrication routes and mechanical properties. Metals 2022;12:1392. https://doi.org/10.3390/met12081392.
[16] Szałapak J, Kiełbasiński K, Dybowska-Sarapuk Ł, Krzeminski J, Teodorczyk M, Kowaluk T, Jakubowska M. Influence of carbon nanoparticles additives on nanosilver joints in LTJT technology. J Electron Packag 2021;143:034501. https://doi.org/10.1115/1.4049240.
[17] Wu L, Qian J, Zhang F, Yu J, Wang Z, Guo H, Chen X. Low-temperature sintering of Cu/functionalized multi-walled carbon nanotubes composite paste for power electronic packaging. IEEE Trans Power Electron 2021:1. https://doi.org/10.1109/TPEL.2021.3103563. 1.
[18] Jeong G-J, Kim T-Y, Lee C, Jung S-B, Kim K-S. Atmospheric plasma-sintered Cu-MWNT nanocomposite films for enhanced thermal management. Surf Interfaces 2025;58:105869. https://doi.org/10.1016/j.surfin.2025.105869.
[19] Wang Z, Zhou M, Lu B, Zhang D, He H. Synthesis of silver Nanoparticle/multi-walled carbon nanotube composites and their application in electronic pastes. Nanomaterials 2025;15:152. https://doi.org/10.3390/nano15030152.
[20] Li H, Zhang X, Feng Y, Zhang X, Qiu L. Constructing non-commensurate Cu–C interfaces with high thermal conductance via symmetric tilt grain boundaries. Carbon Energy 2025;7:e70084. https://doi.org/10.1002/cey2.70084.
[21] Yang Q, Zhu Q, Xu R, Wang D, Miljković M, Zhao H. Molecular interfacial interaction mechanism between Graphene–SBS and bitumen components. Langmuir 2025;41:32885–901. https://doi.org/10.1021/acs.langmuir.5c04980.
[22] Yang Q, Zhu Q, Xu R, Hao L, Lu G, Wang D. Synergism and mechanisms of aging resistance in the use of graphene and carbon nanotubes in bitumen composites. Langmuir 2025;41:842–57. https://doi.org/10.1021/acs.langmuir.4c04182.
[23] Dai J, Wei D, Wang Z, Si L, Cao S, Liu H, Ye Z. Comparative research on atomic diffusion of diamond/Ni and MWCNTs/Ni interfaces with molecular dynamics and experimental methods. Ceram Int 2025;51:5434–50. https://doi.org/10.1016/j.ceramint.2024.12.191.
[24] Cao Z, Yang X, Yang J, Huang X, Ni Y. Reducing Si/Cu interfacial thermal resistance via hybrid CNT-graphene junctions: a molecular dynamics study. Int J Heat Mass Tran 2025;238:126493. https://doi.org/10.1016/j.ijheatmasstransfer.2024.126493.
[25] Zhang Y, Liu Y, Zhao Q, Jiang H, Yu X, Fan Y, Liu Y, Li C, Yi J. Molecular dynamics study of the interface fine structure and mechanical properties of Ni@SWCNT/Cu nanocrystalline composite materials. Mater Sci Eng, A 2024;901:146523. https://doi.org/10.1016/j.msea.2024.146523.
[26] Zhang H-N, Fan Y, Shen H-S. Prediction of temperature-dependent mechanical properties for SWCNT/Cu nanocomposite metamaterials: a molecular dynamics study. Nanomaterials 2023;13:1885. https://doi.org/10.3390/nano13121885.
[27] Zou H, Feng Y, Zhang X, Ohara T, Qiu L. Enhancing mechanism of CNT-CNT interface by metal nanoparticle and nanowire effect on the inside and outside of CNT. Int J Therm Sci 2023;185:108094. https://doi.org/10.1016/j.ijthermalsci.2022.108094.
[28] Song L, Zhao F-Q, Xu S-Y, Ju X-H. Encapsulating aluminum nanoparticles into carbon nanotubes for combustion: a molecular dynamics study. Phys Chem Chem Phys 2021;23:11886–92. https://doi.org/10.1039/D1CP01135A.
[29] Kang Z, Wu B. Coalescence of gold nanoparticles around the end of a carbon nanotube: a molecular-dynamics study. J Manuf Process 2018;34:785–92. https://doi.org/10.1016/j.jmapro.2018.03.051.
[30] Makan M, Makan A, Ghoulbzouri AE. Effect of graphene network reinforcement and interface orientation on the mechanical behavior of nickel composites: a molecular dynamics study. Acta Mater 2025;284:120637. https://doi.org/10.1016/j.actamat.2024.120637.
[31] Lyu H. Low-temperature sinterability of graphene-Cu nanoparticles:molecular dynamics simulations and experimental verification. Appl Surf Sci 2025.
[32] Zhang X, Gao J, Zhang L, Chen Y, Zhang Y, Zhang K. Molecular dynamics study on the sintering mechanism and tensile properties of novel Cu nanoparticle/graphene nanoplatelet composite solder paste. Materials 2024;17:4759. https://doi.org/10.3390/ma17194759.
[33] Holec D, Hartmann MA, Fischer FD, Rammerstorfer FG, Mayrhofer PH, Paris O. Curvature-induced excess surface energy of fullerenes: density functional theory and Monte Carlo simulations. Phys Rev B 2010;81:235403. https://doi.org/10.1103/PhysRevB.81.235403.
[34] Chi X, Zhang J, Nshimiyimana JP, Hu X, Wu P, Liu S, Liu J, Chu W, Sun L. Wettability of monolayer graphene/single-walled carbon nanotube hybrid films. RSC Adv 2017;7:48184–8. https://doi.org/10.1039/C7RA09934G.
[35] Srivastava S, Pandey AK, Dixit CK. Shape and size dependent behaviour of melting temperature for nanoparticles. Natl Acad Sci Lett 2025;48:123–7. https://doi.org/10.1007/s40009-024-01430-3.
[36] Izadi R, Tuna M, Trovalusci P, Fantuzzi N. Bending characteristics of carbon nanotubes: micropolar elasticity models and molecular dynamics simulations. Mech Adv Mater Struct 2023;30:189–206. https://doi.org/10.1080/15376494.2021.2011499.
[37] Williams PL, Mishin Y, Hamilton JC. An embedded-atom potential for the Cu-Ag system. Model Simulat Mater Sci Eng 2006;14:817–33. https://doi.org/10.1088/0965-0393/14/5/002.
[38] Stuart SJ, Tutein AB, Harrison JA. A reactive potential for hydrocarbons with intermolecular interactions. J Chem Phys 2000;112:6472–86. https://doi.org/10.1063/1.481208.
[39] Yousefi P, Abbaspour M, Sokhanvaran V. A comparative study of graphite and CNT supported Au-Ag, Au-Pd, Au-Pt and Au-Rh nanoalloys using MD simulation. J Mol Liq 2019;280:87–96. https://doi.org/10.1016/j.molliq.2019.02.045.
[40] Thompson AP, Aktulga HM, Berger R, Bolintineanu DS, Brown WM, Crozier PS, in 't Veld PJ, Kohlmeyer A, Moore SG, Nguyen TD, Shan R, Stevens MJ, Tranchida J, Trott C, Plimpton SJ. LAMMPS - a flexible simulation tool for particle-based materials modeling at the atomic, meso, and continuum scales. Comput Phys Commun 2022;271:108171. https://doi.org/10.1016/j.cpc.2021.108171.

[41] Stukowski A. Visualization and analysis of atomistic simulation data with OVITO–the Open visualization Tool, Modelling Simul. Mater Sci Eng 2010;18: 015012. https://doi.org/10.1088/0965-0393/18/1/015012.
[42] Chen J, Fan X, Liu J, Gu C, Shi Y, Singh DJ, Zheng W. Heating-Rate and Particle-Size Effects on Melting Process of Au Nanoparticles. J Phys Chem C 2020;124: 7414–20. https://doi.org/10.1021/acs.jpcc.9b10769.
[43] Zhang Q, Wang J, Tang S, Wang Y, Li J, Zhou W, Wang Z. Molecular dynamics investigation of the local structure in iron melts and its role in crystal nucleation during rapid solidification. Phys Chem Chem Phys 2019;21:4122–35. https://doi.org/10.1039/C8CP05654D.
[44] Guo H, Zhang L, Zhu Q, Wang C, Chen G, Zhang P. Molecular dynamics simulation of the coalescence and melting process of Cu and Ag nanoparticles. Adv Condens Matter Phys 2021;2021:1–9. https://doi.org/10.1155/2021/9945723.